

Diffusion-aware voltage source: An equivalent circuit network to resolve lithium concentration gradients in active particles

Mingzhao Zhuo^{a,c,*}, Niall Kirkaldy^a, Tom Maull^b, Timothy Engstrom^b, Gregory Offer^{a,c}, Monica Marinescu^{a,c}

^a*Department of Mechanical Engineering, Imperial College London, London SW7 2AZ, United Kingdom*

^b*WAE Technologies, Wantage OX12 0DQ, United Kingdom*

^c*The Faraday Institution, Didcot OX11 0RA, United Kingdom*

Abstract

Traditional equivalent circuit models (ECMs) have difficulties in estimating battery internal states due to the lack of relevant physics, such as the lithium diffusion in active particles. Here we configure a circuit network to describe the lithium diffusion and define it as a new high-level circuit element called diffusion-aware voltage source. The circuit representation is proven equivalent to the discretized diffusion equation. The new voltage source gives the electrode potential as a function of the surface concentration and thus automatically incorporates the diffusion overpotential. We show that an ECM with the proposed diffusion-aware voltage sources (called “shell ECM”) can reproduce the single particle model simulation results, making it a trustworthy easy-to-implement substitute. Furthermore, the simplest shell ECM consisting of a single diffusion-aware voltage source and a resistor is validated against experimental constant-current discharges at various rates. The diffusion-aware voltage source can be used to measure diffusivity by fitting the diffusion resistance against experimental data. The viability of the shell ECM for onboard usage is confirmed by implementation into a battery management system of WAE Technologies. By tracking the internal concentration states, the shell ECM demonstrates robustness to dynamic applied-current profiles.

Keywords: Diffusion-aware voltage source, equivalent circuit models, single particle model, lithium concentration gradient, solid diffusion

1. Introduction

During (dis)charge of lithium-ion batteries, one of the main limiting physical processes is the slow diffusion of lithium in active material particles [1], impacting battery fast-charge performance [2]. This

*Corresponding author

Email addresses: m.zhuo@imperial.ac.uk, mzhao@connect.ust.hk (Mingzhao Zhuo), n.kirkaldy@imperial.ac.uk (Niall Kirkaldy), Tom.Maull@wae.com (Tom Maull), Timothy.Engstrom@wae.com (Timothy Engstrom), gregory.offer@imperial.ac.uk (Gregory Offer), monica.marinescu@imperial.ac.uk (Monica Marinescu)

Acronyms

ECM	equivalent circuit models	RC	resistor capacitor
PE	positive electrode	NE	negative electrode
OCP	electrode open circuit potential	OCV	cell open circuit voltage
DFN	Doyle-Fuller-Newman (or called P2D)	SPM	single particle model
GITT	Galvanostatic Intermittent Titration Technique	RMSE	root mean square error
SoC	state of charge	BMS	battery management system

Nomenclature

c	concentration variable in active particles	I_{in}	applied current taken by one particle
c_n	average concentration in layer n	τ	diffusion timescale
c_p	lithium concentration in PE particles	R_{ct}	charge-transfer resistance
c_n	lithium concentration in NE particles	C_{dl}	double-layer capacitance
$c_{s,surf}$	particle-surface concentration	R_0	resistance for instantaneous voltage change
$c_{s,max}$	maximum concentration in active particles	R_s	resistance for electronic conduction in the solid
D_s	lithium diffusivity in active particles	R_e	electrolyte resistance
N	maximum number of layers	ϵ_a	volume fraction of active materials
n	layer number ranging from 1 to N	A	total surface area of active materials
a	active-particle radius	V	electrode volume
b	thickness of each layer	N_a	number of active particles
Ω_n	volume of layer n	Q	cell nominal capacity
S_n	outermost surface area of layer n	j	interfacial current density
J_n	lithium mass flux from layer n to $n + 1$	j_0	exchange current density
\bar{I}_n	current flux from layer n to $n + 1$	m	charge-transfer reaction rate
$R_{d,n}$	diffusion resistance between layer n and $n + 1$	η	reaction overpotential
V_n	voltage of voltage source n	S_a	particle surface area to volume ratio
V_t	cell terminal voltage	F	Faraday constant
I_n	current flowing into voltage source n	R	gas constant
k	constant coefficient for unit conversion	T	absolute temperature
I_{app}	applied current		

mechanism has been well considered in physics-based models such as the widely-used Doyle-Fuller-Newman (DFN) model [3]; however, it is not sufficiently described in traditional equivalent circuit models (ECMs). Traditional ECMs account for the diffusion-induced overpotential by a series of resistor-capacitor (RC) pairs but cannot capture the internal concentration states, especially the particle surface concentration for state of available power (SoAP) estimation. Here, we propose a circuit network consisting of diffusion resistors and voltage sources to describe the solid diffusion process and resolve lithium concentration distribution to assist internal state estimation and battery control.

The fundamental physical processes in lithium-ion batteries include lithium diffusion in active materials, lithium-ion diffusion and migration in the electrolyte, electronic conduction in the solid conductive materials, and intercalation chemical reactions at the solid-electrolyte interface. These processes are well understood and described in the DFN model by partial differential algebraic equations (PDAEs), leading to accurate prediction of battery behavior and estimation of internal states. Besides these basic physical processes, other physics such as thermal behavior and battery ageing from side reactions have also been modeled by mathematical equations added to the DFN model. However, discretizing and solving the coupled PDAEs for battery composite materials are costly in terms of implementation and computation, and thus physics-based models are often infeasible for real-time application in state-of-art battery control systems.

In contrast, ECMs leverage well-established knowledge of electrical circuits (e.g., resistors, capacitors, and voltage sources) to mimic the cell behavior, in place of modelling the underlying physics. The standard electrical elements allow the ECMs to be solved in real time so that ECMs are widely used in battery management systems (BMS) for control purpose. However, the loss of connection to physical processes also hinders ECMs in internal state estimation and weakens their prediction power. For example, the electrode open circuit potential (OCP) is a function of the surface concentration, and both the electrode OCP and surface concentration change during the cell rest following a charge/discharge due to the solid diffusion. Traditional ECMs use a Warburg resistance [1] to represent the solid diffusion effect and then approximate it with multiple (usually two) RC pairs. Although the RC pair has a characteristic time constant and can model the voltage change, it is still not aware of the concentration distribution in the particle and on the surface.

The surface concentration is different from the average concentration as the slow diffusion leads to concentration gradients, especially under high dis(charge) rates. It cannot be directly measured or estimated from the measured current and voltage data. However, it is an important internal state in model-based battery control, for example, in the design of fast-charge protocols [4] and in accurate SoAP estimation [5, 6] for fast-discharge applications.

Continuous efforts [7–13] have been made in bringing physics into circuit-based models for better state estimation and more accurate prediction. The common idea is to use electrical analogies to represent the physical processes, including ageing mechanisms. Most of these works focused on converting the DFN model into an equivalent circuit-based model, addressing the current distribution and charge transport processes. The solid diffusion effect was addressed quite differently among the existing studies. The first approach [11, 13] is to solve the continuous diffusion equation using numerical techniques such as finite difference method and then use the solved surface concentration to calculate the electrode potential. Alternatively, Li et al. [12] used a two-parameter polynomial approximation to the numerical solution to obtain the surface potential, which is a common approximation technique for single particle models [14]. Furthermore, Ouyang et al. [15] and Zheng et al. [16] disregarded the concentration distribution, but estimated the surface concentration from available approximate solutions to the diffusion equation. A circuit-style approach is to use circuit networks comprising of resistors and capacitors [7, 9] or of resistors and voltage sources [10] to mimic the solid diffusion process. However, transforming the diffusion process from physical description to circuit arrangement has still not been addressed in a satisfactory way. The numerical solutions [11, 13] or approximate solutions [12, 15, 16] appear to have the same level of implementation complexity as physics-based models. The circuit networks for solid diffusion in Merla et al. [10] used the electrode OCP, rather than concentration gradients, as the driving force for diffusion. The resistor-capacitor networks [7, 9] proposed promising analogies but needed further improvement.

A well-designed circuit representation implementing the correct solid diffusion physics is needed for ECMs to be easily parameterized and implemented in a real-world BMS. To this end, we propose a circuit network (Section 2.2), consisting of controlled voltage sources and diffusion resistors, and define it as a new circuit element called diffusion-aware voltage source (Fig. 3). An ECM involving the diffusion-aware voltage sources, called “shell ECM” (Section 2.3), is configured to predict cell responses. The proposed diffusion-aware voltage source and shell ECMs are verified (Section 3) against the physics-based single particle model run in an open-source battery-modelling toolbox PyBaMM [17]. The shell ECM is further validated against experimental data in Section 4. Finally, the shell ECM is implemented into the BMS of WAE Technologies and compared with traditional ECMs in terms of computational efficiency and accuracy (Section 5).

2. Equivalent circuit network for solid diffusion

In this section, we present an equivalent circuit network for solid diffusion in active particles and then define the proposed equivalent circuit network as a diffusion-aware voltage source that can be used to

configure physics-informed ECMs. We start with a brief introduction to the continuous description of the solid diffusion and its spatial discretization by finite volume method in Section 2.1. Based on the spatially discretized diffusion equation, we devise the diffusion-aware voltage source (Section 2.2) and propose battery-cell ECMs with the new voltage sources (Section 2.3), hereafter called shell ECMs.

2.1. Preliminaries: diffusion equation and its discretization

The transport of intercalated lithium in active particles is often described, under the assumption of Fickian diffusion [18], by a partial differential equation that is expressed as

$$\frac{\partial c}{\partial t} + \nabla \cdot (-D_s \nabla c) = 0, \quad (1)$$

where c is the field variable of lithium concentration and D_s is the diffusivity coefficient. Assuming spherical active particles, we reduce by symmetry the diffusion equation (1) to

$$\frac{\partial c}{\partial t} + \frac{1}{r^2} \frac{\partial}{\partial r} \left(-r^2 D_s \frac{\partial c}{\partial r} \right) = 0, \quad (2)$$

where r denotes the radial direction (Fig. 1) in a spherical coordinate system. The boundary conditions at the particle center and surface are, respectively,

$$\left. -D_s \frac{\partial c}{\partial r} \right|_{r=0} = 0 \quad \text{and} \quad \left. -D_s \frac{\partial c}{\partial r} \right|_{r=a} = j/F, \quad (3)$$

where j is the interfacial current density flowing out the particle and a is the particle radius.

Following the finite volume method, we divide the sphere into N layers of equal thickness, as shown in Fig. 1, and integrate Eq. (2) over an arbitrary layer n (control volume):

$$\int_{r_{n-1}}^{r_n} 4\pi r^2 \left[\frac{\partial c}{\partial t} + \frac{1}{r^2} \frac{\partial}{\partial r} \left(-r^2 D_s \frac{\partial c}{\partial r} \right) \right] dr = 0. \quad (4)$$

The concentration variable c in layer n is considered constant and equal to the average concentration denoted as c_n . We thus have

$$\frac{\partial c_n}{\partial t} \Omega_n + S_n J_n - S_{n-1} J_{n-1} = 0, \quad (5)$$

where Ω_n represents the volume of layer n , S_n is the outermost surface area of layer n , and J_n denotes the

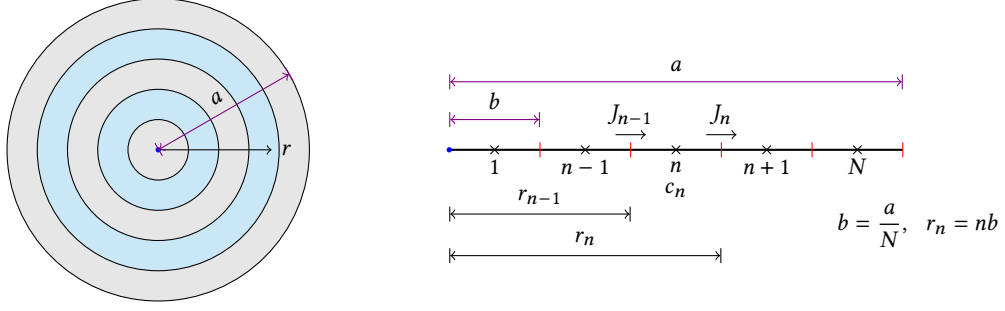


Fig. 1. Schematics of discretizing an active particle of radius a . The particle is discretized into N layers with layer number n ranging from 1 to N . The symbol J_n denotes mass flux from layer n to $n + 1$, and c_n is the lithium concentration in layer n .

flux at the outermost surface:

$$\Omega_n = \frac{4}{3}\pi(r_n^3 - r_{n-1}^3), \quad S_n = 4\pi r_n^2, \quad J_n = -D_s \frac{\partial c}{\partial r} = -D_s \frac{c_{n+1} - c_n}{b}, \quad (6)$$

where b is the thickness of each layer. Inserting Eq. (6) into Eq. (5), we obtain the mass conservation for an arbitrary layer n :

$$\frac{dc_n}{dt} \Omega_n = \frac{c_{n+1} - c_n}{b/(S_n D_s)} - \frac{c_n - c_{n-1}}{b/(S_{n-1} D_s)}. \quad (7)$$

2.2. Equivalent circuit representation

In traditional ECMs, solid diffusion in active particles is modeled by a Warburg element and a finite number of RC pairs [1], which can mimic the voltage response of a cell under certain conditions but cannot resolve the concentration gradient inside a particle. In particular, the surface concentration and real electrode potential cannot be obtained for improved state estimation. Here we use electrical analogies to describe the solid diffusion and configure voltage sources and resistors in a shell structure as shown in Fig. 2, in place of the differential equation description Eq. (2).

In the shell circuit network (Fig. 2), we have two electrical elements: resistors and controlled voltage sources. The voltage source V_n corresponds to the layer n in Fig. 1 on a one-to-one basis. According to Kirchhoff's voltage law, for an arbitrary circuit loop in Fig. 2a we have

$$V_n = V_{n+1} + \bar{I}_n R_{d,n}. \quad (8)$$

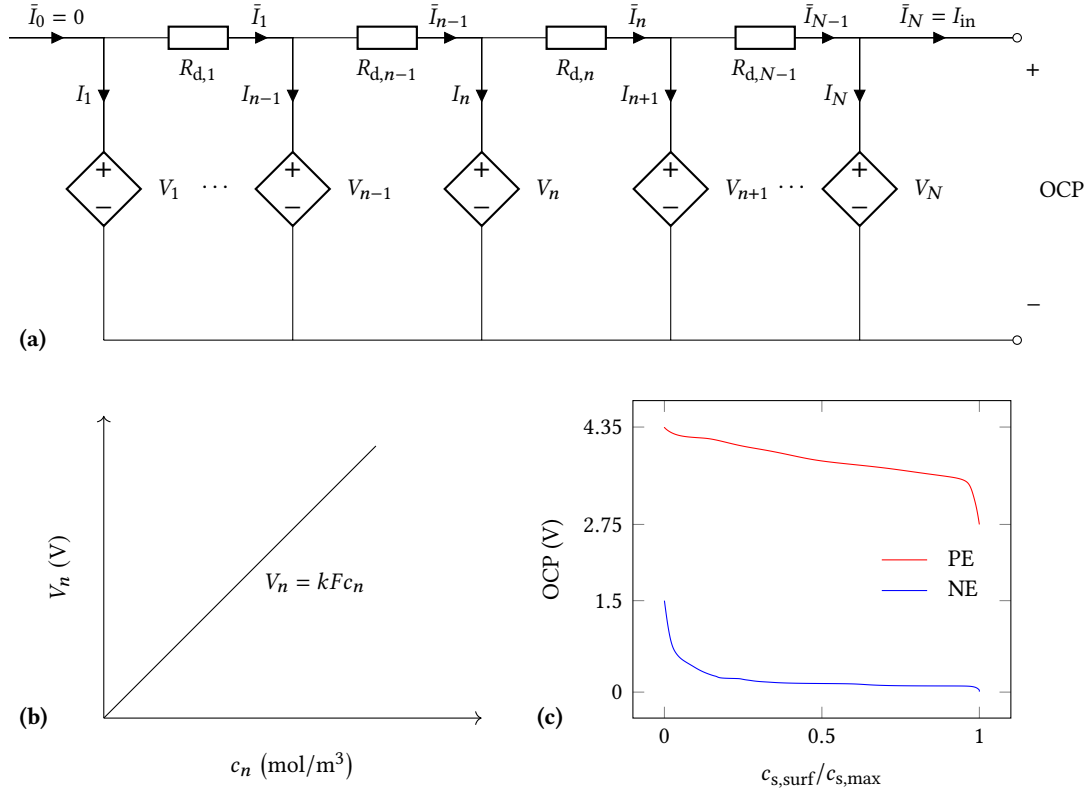


Fig. 2. Schematics of shell circuit network (a) for solid diffusion description. The voltage V_n ($n = 1, 2, \dots, N$) of an arbitrary layer n is a linear function of its internal state—lithium concentration c_n , as shown in (b). The open circuit potential (OCP) of the particle depends on the surface concentration normalized by the maximum concentration $c_{s,\text{surf}}/c_{s,\text{max}}$. The real OCP relations for the positive electrode (PE) and negative electrode (NE) of a LG M50 cell [19] are shown in (c) as an example.

Kirchhoff's current law states that

$$I_n = \bar{I}_{n-1} - \bar{I}_n. \quad (9)$$

Calculating \bar{I}_{n-1} and \bar{I}_n from Eq. (8) and inserting them into Eq. (9), we have

$$I_n = \frac{V_{n-1} - V_n}{R_{d,n-1}} - \frac{V_n - V_{n+1}}{R_{d,n}}. \quad (10)$$

For each layer n , we further attach an internal state variable c_n quantifying the local lithium concentration to the controlled voltage source V_n and define the controlled voltage as

$$V_n = kFc_n, \quad (11)$$

where F is Faraday's constant and k ($\text{V m}^3/\text{C}$) is a constant coefficient to make units consistent in the left- and right-hand sides of Eq. (11). The value of k has no impact and thus is set to be 1 hereafter. Substituting Eq. (11) into Eq. (10), we have

$$\frac{I_n}{F} = \frac{c_{n+1} - c_n}{R_{d,n}/k} - \frac{c_n - c_{n-1}}{R_{d,n-1}/k}. \quad (12)$$

The current flow I_n in Fig. 2 means charge flux into voltage source V_n , and this is analogous to the lithium mass flux into layer n . To draw the analogy, we use Faraday's constant F to make the units consistent:

$$\frac{I_n}{F} = \frac{dc_n}{dt} \Omega_n, \quad (13)$$

indicating that the left-hand sides of Eq. (7) and Eq. (12) are equal. We can further define the diffusion resistances in the shell circuit network as

$$R_{d,n} = \frac{kb}{S_n D_s} = \frac{kb}{4\pi(nb)^2 D_s} = \frac{kN}{4\pi n^2 a D_s}. \quad (14)$$

Now Eqs. (7) and (12) are completely equivalent. Therefore, with the definition of controlled voltage source in Eq. (11) and diffusion resistance in Eq. (14), the proposed shell circuit network is equivalent to the spatially discretized diffusion equation. We remark that the driving force of current flow is the voltage difference and this reflects that the concentration gradient is the driving force for diffusion. The governing equations for the shell circuit network are summarized in Table 1, and the numerical techniques to solve them can be

Table 1. Governing equations for the diffusion-aware voltage source.

1. Kirchhof's voltage law:

$$V_n = V_{n+1} + \bar{I}_n R_{d,n}, \quad n = 1, 2, \dots, N - 1 \quad (8)$$

2. Kirchhof's current law:

$$I_n = \bar{I}_{n-1} - \bar{I}_n, \quad n = 1, 2, \dots, N \quad (9)$$

3. Internal state evolution:

$$\frac{dc_n}{dt} = \frac{1}{F\Omega_n} I_n(t), \quad n = 1, 2, \dots, N \quad (13)$$

4. Constitutive relation:

$$V_n = kFc_n, \quad n = 1, 2, \dots, N \quad (11)$$

found in [Appendix A](#).

The integral form of the internal state c_n of layer n can be derived from Eq. (13):

$$c_n = c_{n,0} + \frac{1}{F\Omega_n} \int_{t_0}^t I_n dt, \quad (15)$$

where $c_{n,0}$ represents the initial state, corresponding to the initial condition of diffusion equation (2) that is omitted for brevity. Finally, the two current flows at the edges of the shell circuit network are specified as

$$\bar{I}_0 = 0 \quad \text{and} \quad \bar{I}_N = I_{\text{in}}, \quad (16)$$

where I_{in} is the portion of applied current I_{app} for one active particle (detailed below). These two expressions correspond to the boundary conditions (3) of the diffusion equation.

The shell circuit network as a whole can be considered as a high-level circuit element whose input is the applied current. The output is the electrode potential

$$\text{OCP} = \text{OCP}(c_{\text{s,surf}}), \quad (17)$$

where OCP is the measured potential function for an active material (see Fig. 2c for examples) and the

surface concentration is linearly extrapolated from those of the outermost two layers

$$c_{s,\text{surf}} = 1.5c_N - 0.5c_{N-1}. \quad (18)$$

In Fig. 2, there are $N - 1$ diffusion resistors, but only one resistance is unknown and needs to be determined. According to Eq. (14), the innermost resistance is the largest and thus is chosen as the unknown and the baseline for calculating other diffusion resistances. It can be expressed as

$$R_{d,1} = \frac{kN}{4\pi a D_s}. \quad (19)$$

We remark that the diffusion resistance is inversely proportional to the solid diffusivity, and this relation can be used, as an alternative to the current approach [20], to measure the diffusivity of active materials in the laboratory (Appendix C), being the diffusion resistance fitted from experimental data. The shell circuit network is designed for the physical process of diffusion, and thus there must be a timescale associated with it. We define the timescale of the shell circuit network as that associated with the continuous diffusion equation:

$$\tau = \frac{a^2}{D_s} = \frac{4\pi a^3 R_{d,1}}{kN}, \quad (20)$$

where the diffusivity D_s is expressed in terms of diffusion resistance $R_{d,1}$ from Eq. (19).

2.3. Shell equivalent circuit model

In the previous section, we devise a circuit network for the solid diffusion. This network can be considered as a new high-level circuit element that takes current as the input, stores internal states of concentration (or local SoC), and gives surface OCP as the output. Thus, we define it as a diffusion-aware voltage source symbolized by a double-wall diamond as shown in Fig. 3.

Based on the diffusion-aware voltage source, we propose an ECM in Fig. 3a to resolve the fundamental physical processes described in the DFN model (detailed in Introduction) and call it the comprehensive shell ECM. The comprehensive shell ECM consists of two similar sub-circuits in the left-hand and right-hand sides, corresponding to the negative electrode (NE) and positive electrode (PE), respectively. The upper resistors R_s are used to model the electrical potential variation in the electrode thickness direction due to the electronic current flow in solid conductive materials. The lower resistors R_e are designed for the overpotential caused by lithium-ion transport in the electrolyte. Connecting electronic and ionic current flows is the intercalation and deintercalation chemical reactions on the active particle surface, represented

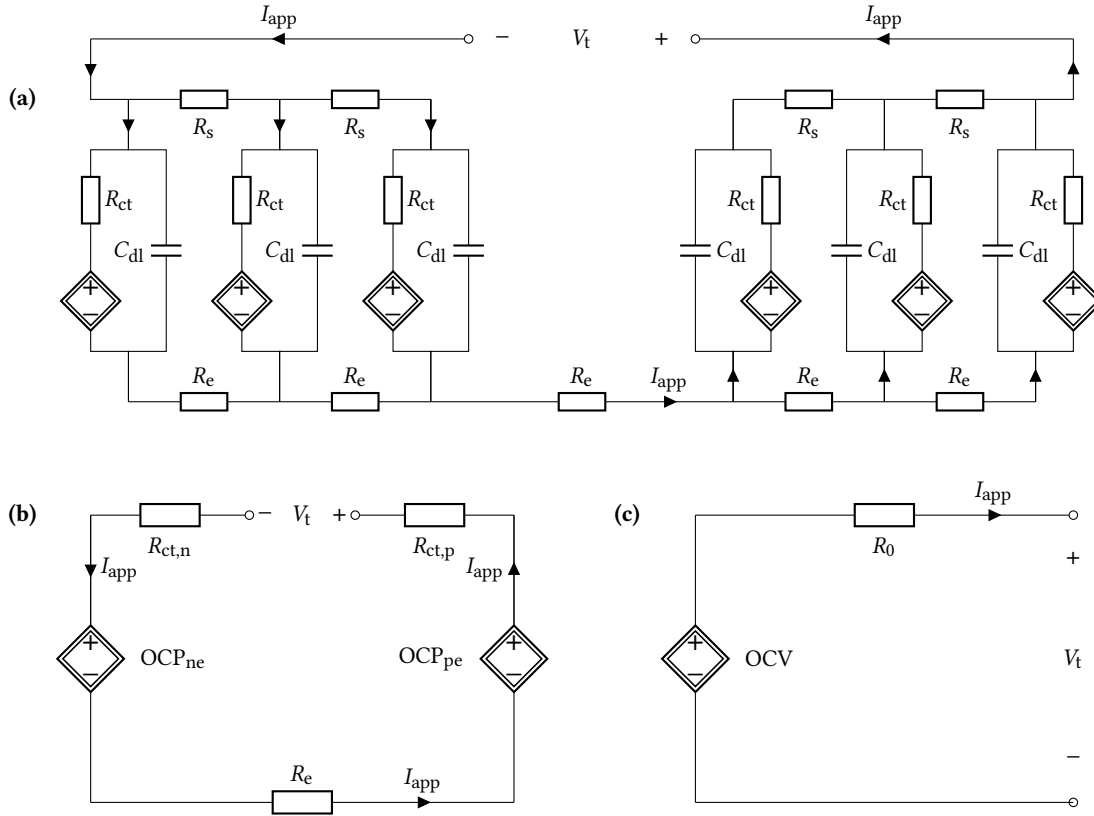


Fig. 3. Shell ECMs equivalent to physics-based models—the DFN model (a) and Single Particle Model (b). Further simplified shell ECM (c) for easy experimental parameterization. The diffusion-aware voltage source (double-wall diamond symbol) represents the proposed shell circuit network in Fig. 2.

by an elementary circuit unit involving a double layer capacitor C_{dl} , a charge transfer resistance R_{ct} , and the diffusion-aware voltage source. This elementary circuit unit resembles the Randles circuit [1] but replaces the Warburg impedance with the newly defined diffusion-aware voltage source.

In Fig. 3a, we only show for demonstration three elementary circuit units in parallel at each side; the more elementary units, the higher the resolution of current distribution and lithium concentration gradient across the electrode thickness. The comprehensive shell ECM is thus especially suitable for high-current (dis)charges. For better interpretation of the diffusion-aware voltage source, we simplify the shell ECM to the extent shown in Fig. 3b. We first disregard R_s and R_e as the electronic and ionic conduction are fast and the corresponding overpotentials are relatively small [13]. Then, we omit the double-layer capacitance as it has very little impact except at very high frequencies [1]. Consequently, the three elementary circuit units within each electrode would behave identically and thus can be integrated into one.

We remark that the simplification from (a) to (b) is based on the assumption that all particles in different locations of the electrode behave identically, rather than made by using one particle to replace all the particles [21]. Therefore, the applied current I_{app} needs to be shared by all active particles, and the input current I_{in} for the diffusion-aware voltage source should be calculated as

$$I_{in} = I_{app}/N_a, \quad (21)$$

where N_a is the number of active particles.

The simplified shell ECM in Fig. 3b captures all the physics of the single particle model (SPM)—lithium diffusion in an active particle and charge transfer overpotential—and thus can fully reproduce the SPM simulation results. Moreover, it involves R_e to model the electrolyte resistance within the separator.

In practice, the measured cell data do not distinguish between the NE and PE. Thus, we further simplify the shell ECM in Fig. 3b to the one in Fig. 3c. The resistance R_0 responsible for instantaneous voltage change includes the transport resistance in the whole cell including the electrolyte and electronically-conductive materials. The diffusion-aware voltage source combines the diffusion effects of the PE and NE. It is noteworthy that this ECM has only 2 parameters to calibrate: R_0 and $R_{d,1}$.

Finally, the terminal voltages for shell ECMs in Fig. 3b and c are calculated, respectively, as

$$V_t = OCP_{pe} - OCP_{ne} - I_{app}(R_{ct,p} + R_{ct,n} + R_e), \quad (22a)$$

$$V_t = OCV - I_{app}R_0. \quad (22b)$$

Table 2. Parameters of a LG M50 cell [19] for simulations in Section 3.

Parameter	symbol	unit	value	
			positive electrode	negative electrode
particle radius	a	μm	5.22	5.86
maximum lithium concentration	$c_{s,\text{max}}$	mol/m^3	63104	33133
initial concentration	$c_{s,0}$	mol/m^3	17 038	29 866
active material volume fraction	ϵ_a	-	0.665	0.75
diffusivity	D_s	m^2/s	4×10^{-15}	3.3×10^{-14}
charge-transfer reaction rate	m	$\text{Am}^{2.5}\text{mol}^{-1.5}$	3.42×10^{-6}	6.48×10^{-7}
electrode volume	V	m^3	7.764×10^{-6}	8.75×10^{-6}
open circuit potential	OCP	V	Fig. 2c	Fig. 2c
cell nominal capacity	Q	A h	5	
coefficient for unit conversion	k	$\text{V m}^3/\text{C}$	1	
lithium-ion concentration in electrolyte	c_e	mol/m^3	1000	
Faraday constant	F	C/mol	96 485	
gas constant	R	$\text{J}/(\text{K mol})$	8.31	
absolute temperature	T	K	298.15	

3. Comparison with physics-based model

This section aims to verify the developed diffusion-aware voltage source by comparing its simulation results with results of a physics-based model simulation. Specifically, we first validate the equivalence between the diffusion-aware voltage source (Fig. 2) and the solid diffusion equation and verify its numerical implementation in Section 3.1, and then in Section 3.3 we extend the verification to the shell ECM (Fig. 3b). For simplicity, we choose the SPM and run it within PyBaMM [17] as the reference solution. In the PyBaMM simulation, we pick the LG M50 cell with a parameter set characterized by Chen et al. [19]. The parameters needed for simulations in this section can be found in Table 2.

3.1. Diffusion-aware voltage source

To check the ability of the diffusion-aware voltage source in resolving the lithium concentration, we simulate the response of a cell subjected to a sequence of constant-current discharge, rest, constant-current charge, and rest and monitor the concentration variation in the PE. The choice of the PE is because that it has lower diffusivity than the NE. The test protocol can be confirmed by the current profile in Fig. 4a, where the sign of current is positive on discharge. From the PyBaMM simulation of SPM, we can retrieve the lithium concentration profiles (Fig. 4b) at different time instants, the PE particle surface concentration evolution (Fig. 4b), and the PE open circuit potential (Fig. 4d) and use them to check the diffusion-aware voltage source response.

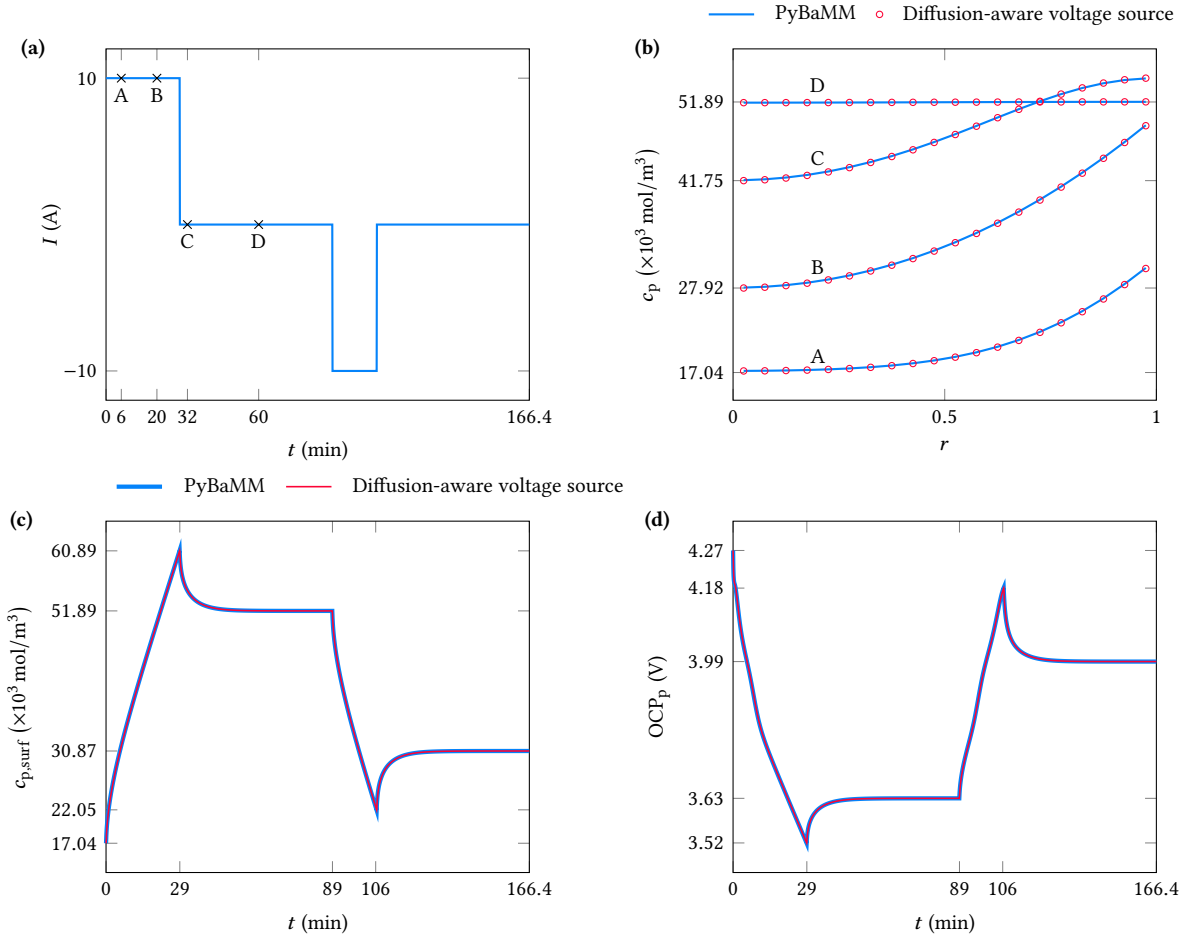


Fig. 4. Verification of the diffusion-aware voltage source by comparing with PyBaMM simulation results. Subplot (a) shows the current profile of the test of discharge, rest, charge, and rest, and subplot (b) shows the concentration c_p profiles of the positive electrode (PE) at 4 time instants A-D pinpointed in (a). Subplots (c) and (d) show the surface concentration $c_{p,surf}$ of the PE active particle and the corresponding PE open circuit potential (OCP_p).

For a fair comparison, the same parameter values as in the SPM are used in the diffusion-aware voltage source (Fig. 2a). Specifically, the following parameters are needed: particle radius a , diffusivity D_s , initial concentration $c_{s,0}$, and the number of particles N_a . The number of active particles is determined by two more parameters:

$$N_a = \frac{\epsilon_a V}{4\pi a^3/3}, \quad (23)$$

where V is the electrode volume and ϵ_a is the volume fraction of active material.

We pick four time instants (A-D) during the discharge and the following relaxation process and show the concentration spatial distribution for comparison in Fig. 4b. The surface concentration is calculated by Eq. (18) and presented in Fig. 4c as a function of time. Based on the surface concentration, the PE OCP is calculated according to the same function in the SPM. The agreement in Fig. 4b-d verifies the equivalence between the proposed circuit network and the discretized diffusion equation as well as the numeric implementation of the circuit network. We remark that this equivalence holds regardless of the applied currents and usage scenarios.

3.2. Charge transfer resistance

With the diffusion-aware voltage source verified, we further explore the possibility of reproducing the SPM using an ECM (Fig. 3b) incorporating the diffusion-aware voltage source. Besides the diffusion overpotential, another major contribution to terminal voltage loss in the SPM comes from the reaction overpotential. The reaction overpotential in the SPM does not involve a timescale, and thus we simply use a resistor with varying resistance to reproduce the same effect.

To obtain this charge transfer resistance, we first calculate the reaction overpotential by reversing the Butler-Volmer equation [22] that describes the electrochemical reaction at the active particle surface. According to Butler-Volmer equation, the interfacial current density j is expressed as [21]

$$j = 2j_0 \sinh\left(\frac{F\eta}{2RT}\right), \quad (24)$$

where j_0 is the exchange current density and η is the reaction overpotential. In the SPM, the interfacial current density is determined from the applied current I_{app} via

$$j = \frac{I_{app}}{A} = \frac{I_{app}}{3\epsilon V/R} = \frac{I_{app}}{S_a \epsilon V}, \quad (25)$$

where A is the total surface area of active materials, $S_a = 3/R$ denotes the particle specific area (surface

area to volume ratio), ϵ is the active material volume fraction, and V represents the electrode volume. The inverse Butler-Volmer relation is then formulated to express the reaction overpotential η , and the charge transfer resistance is then calculated as

$$R_{\text{ct}} = \frac{\eta}{I_{\text{app}}} = \frac{2RT}{FI_{\text{app}}} \operatorname{arcsinh}\left(\frac{j}{2j_0}\right) = \frac{2RT}{FI_{\text{app}}} \operatorname{arcsinh}\left(\frac{I_{\text{app}}}{2j_0 S_a \epsilon V}\right). \quad (26)$$

Here, the exchange current density j_0 is written as [21]

$$j_0 = m \sqrt{c_{\text{s,surf}}(c_{\text{s,max}} - c_{\text{s,surf}})c_{\text{e}}}, \quad (27)$$

where m ($\text{A}/\text{m}^2 \cdot (\text{m}^3/\text{mol})^{1.5}$) is a rate constant of the charge transfer reaction, $c_{\text{s,max}}$ is the maximum lithium concentration in the active particle, $c_{\text{s,surf}}$ is the surface concentration of the active particle, and c_{e} is the lithium-ion concentration in the electrolyte. In the SPM, the lithium-ion concentration in electrolyte is simplified as a constant, and thus the exchange current density $j_0(c_{\text{s,surf}})$ is only a function of particle surface concentration $c_{\text{s,surf}}$. Finally, we remark that R_{ct} in Eq. (26) expresses the equivalent resistance of the charge transfer resistors of all particles within each electrode arranged in parallel because the applied current is assumed to be shared by all particles equally.

The inverse hyperbolic sine function $\operatorname{arcsinh}(x)$ approaches x as x tends to 0, i.e.,

$$\lim_{x \rightarrow 0} \frac{\operatorname{arcsinh}(x)}{x} = 1. \quad (28)$$

Hence, at low currents, we approximate $\operatorname{arcsinh} \approx x$, and Eq. (26) is further simplified as [13]

$$R_{\text{ct}} \approx \frac{RT}{F j_0 S_a \epsilon V}. \quad (29)$$

In this case, the charge transfer resistance is solely determined by the particle surface concentration (the electrolyte concentration c_{e} in Eq. (27) is assumed constant in the SPM; see Table 2). The particle surface concentration is time-varying, so is the charge transfer resistance.

To check the effect of applied current magnitude, we calculate the charge transfer resistance at different C-rates as shown in Fig. 5. In general, the resistance of the NE is an order of magnitude larger than that of the PE (caused by the reaction constant m in Eq. (27)), and the effect of the applied current is more significant for the NE. For both electrodes, the approximation at small currents overestimates the resistance.

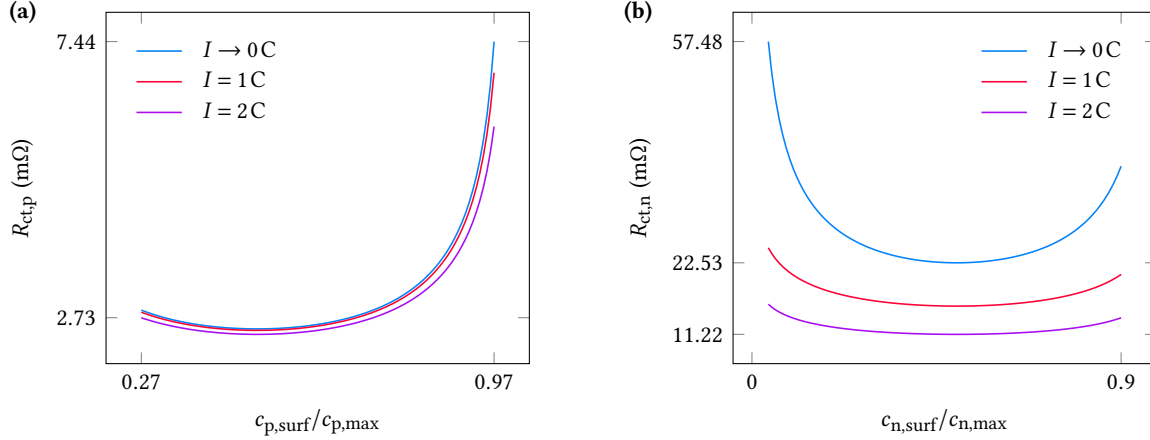


Fig. 5. Charge transfer resistance in the positive ($R_{ct,p}$) and negative ($R_{ct,n}$) electrodes as function of surface concentration at different C-rates.

3.3. Shell ECM

We further compare the shell ECM (Fig. 3b) against the SPM. For the shell ECM, the electrolyte resistance R_e is set to be null, and charge transfer resistances $R_{ct,n}$ and $R_{ct,p}$ are determined through Eq. (26). Three typical test profiles are considered: a discharge-rest-charge-rest cycle (same as in previous section), Galvanostatic Intermittent Titration Technique (GITT), and constant-current discharges at varying current rates. Fig. 6 shows the terminal voltage obtained from running the shell ECM and the PyBaMM SPM simulation with the same parameters. It is shown that the shell ECM can completely reproduce the SPM simulation results.

4. Experimental validation

This section aims to validate the proposed shell ECM by comparison with experimental measurements of LG M50T cells. In real-world applications, the terminal voltage is often measured for the whole cell without differentiating the contributions from the two electrodes. Thus, we choose the simplified shell ECM involving a single diffusion-aware voltage source as shown in Fig. 3c.

For parameterization and validation, GITT and constant-current discharge tests were performed respectively on the LG M50T cells. Before these tests, the cells were fully charged through the constant-current/constant-voltage protocol at a charge rate of 0.3 C to a maximum voltage of 4.2 V until a cut-off current of C/100, followed by a two-hour rest. The GITT tests consists of 25 repeating segments of a discharge pulse at a 1 C rate for 144 seconds followed by a one-hour rest. The cell nominal capacity is 5 A h, and thus each discharge pulse consumes a capacity of 0.2 A h. Constant-current discharge tests were conducted at rates of 0.4 C and 2 C until the lower voltage limit of 2.5 V was reached. All tests were

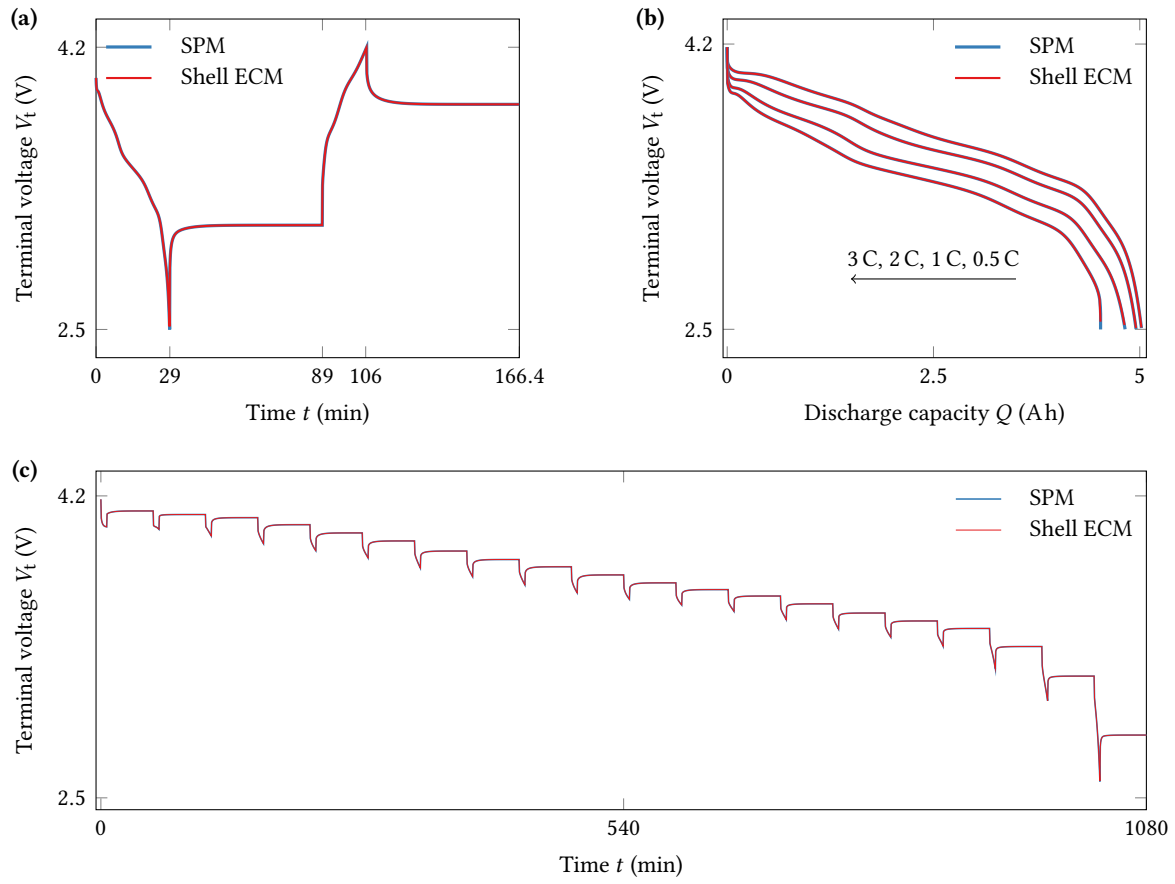


Fig. 6. Comparison between shell ECM results and results from SPM simulation in PyBaMM in terms of terminal voltage for three test protocols.

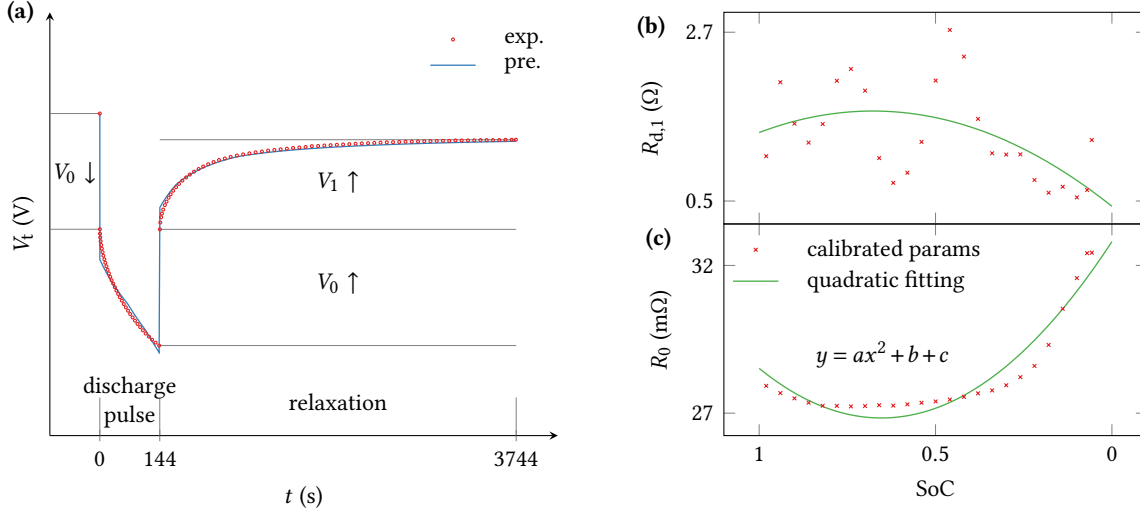


Fig. 7. The two shell-ECM parameters are determined for each discharge-rest segment. (a) A typical discharge pulse at a 1 C rate followed by a rest where the two parameters are assumed constant. (b) Calibrated parameters for 25 discharge-rest segments and the second-order polynomial fitting of these parameters as function of the state of charge (SoC) for model prediction in the following constant-current discharges. The SoC of each point takes the mean value of the SoC range that the corresponding discharge-rest segment goes through.

performed at a temperature of 25 °C in a thermal chamber. Full details of the experimental procedures, apparatus, and thermal management can be found in [Appendix B](#).

The shell ECM is first parameterized using the GITT data and then used to predict the cell performance under constant-current discharge conditions. The model predictions are compared with the measurements.

4.1. Parameterization

For the shell ECM in Fig. 3c, there are only two parameters to be calibrated: the ohmic resistance R_0 and the diffusion resistance $R_{d,1}$ between the first and the second layers (Fig. 2). These two parameters are determined from the GITT data on a pulse-by-pulse basis as sketched in Fig. 7a. For each discharge pulse followed by a rest, the two parameters are assumed constant and are identified separately. The ohmic resistance R_0 is determined from the instantaneous drop and increase of the terminal voltage V_0 divided by the applied current, and the average of the two R_0 values is recorded. The diffusion resistance $R_{d,1}$ is fitted by minimizing the difference between the experimental measurements and model prediction of the terminal voltage (i.e., least-squares method). The least-squares fitting is only applied to the relaxation section in Fig. 7a where the ohmic effect vanishes.

The calibrated parameters for each discharge-rest segment are then presented as discrete points in Fig. 7b and c. Each discharge pulse undergoes 144 s at a 1 C rate and corresponds to 4% of the cell nominal capacity. Thus, there are in total 25 discharge pulses and corresponding parameter sets. The cell average

SoC is calculated by Coulomb counting and its variation during each discharge pulse is recorded. The mean value of the two SoC limits of each pulse is then used to indicate the SoC level associated with the calibrated parameters.

With the two parameters identified for each segment, the best-fitting voltage curve is shown in comparison with the experimental curve in Fig. 8a. Also, the equilibrium points after relaxation are taken to serve as the OCV. To evaluate the calibration, we plot the root mean square error (RMSE) for each discharge-rest segment in Fig. 8b:

$$\text{RMSE} = \sqrt{\frac{1}{J} \sum_{j=1}^J (V_{\text{exp},j} - V_{\text{pre},j})^2}, \quad (30)$$

where j represents the j -th point and J is the number of data points. Here we present two RMSE curves: one takes data of the whole discharge-rest segment, indicating the overall error of calibrating R_0 and fitting $R_{d,1}$; the other only uses the data of the rest section, indicating the least-squares fitting error. Compared to the overall error, the fitting error of $R_{d,1}$ is relatively small, implying that the relaxation process through diffusion is well modeled. Another observation in Fig. 8b is that the fitting errors in the low SoC area (pulses 23–25) are higher than those for other pulses. This observation suggests that the poor estimation accuracy is not likely to be improved by considering the solid diffusion and resolving surface concentration for the LG M50T cells, different from the conclusion by Ouyang et al. [15].

According to Eq. (20), the timescale of solid diffusion is related to the diffusion resistance $R_{d,1}$. Here, the diffusion resistance $R_{d,1}$ is fitted from experimental data and reflects the collective effect of diffusion in both electrodes. In general, the NE has diffusivity one order of magnitude higher than that of the PE [19], that is, the diffusion in the PE is the limiting process. We thus assume that the fitted resistance mainly indicates the PE diffusion timescale, and the timescale is then estimated as

$$\tau_{\text{fit}} = \frac{4\pi a^3 F c_{s,\text{max}} N_a}{kN} R_{d,1}, \quad (31)$$

where N_a is the particle number calculated by Eq. (23) and N is the number of layers of the diffusion-aware voltage source (Fig. 3c). The derivation of Eq. (31) can be found in Appendix C. The fitted timescale τ_{fit} would not change too much if the parameter set of NE is used, in view of the consistency between both electrodes in terms of capacity ($\sim c_{s,\text{max}} a^3 N_a$).

The fitted timescales at different SoC levels basically remain at the same magnitude and generally higher than the value of 1.89 h calculated from PE particle radius and diffusivity of a LG M50 cell [19]. We remark

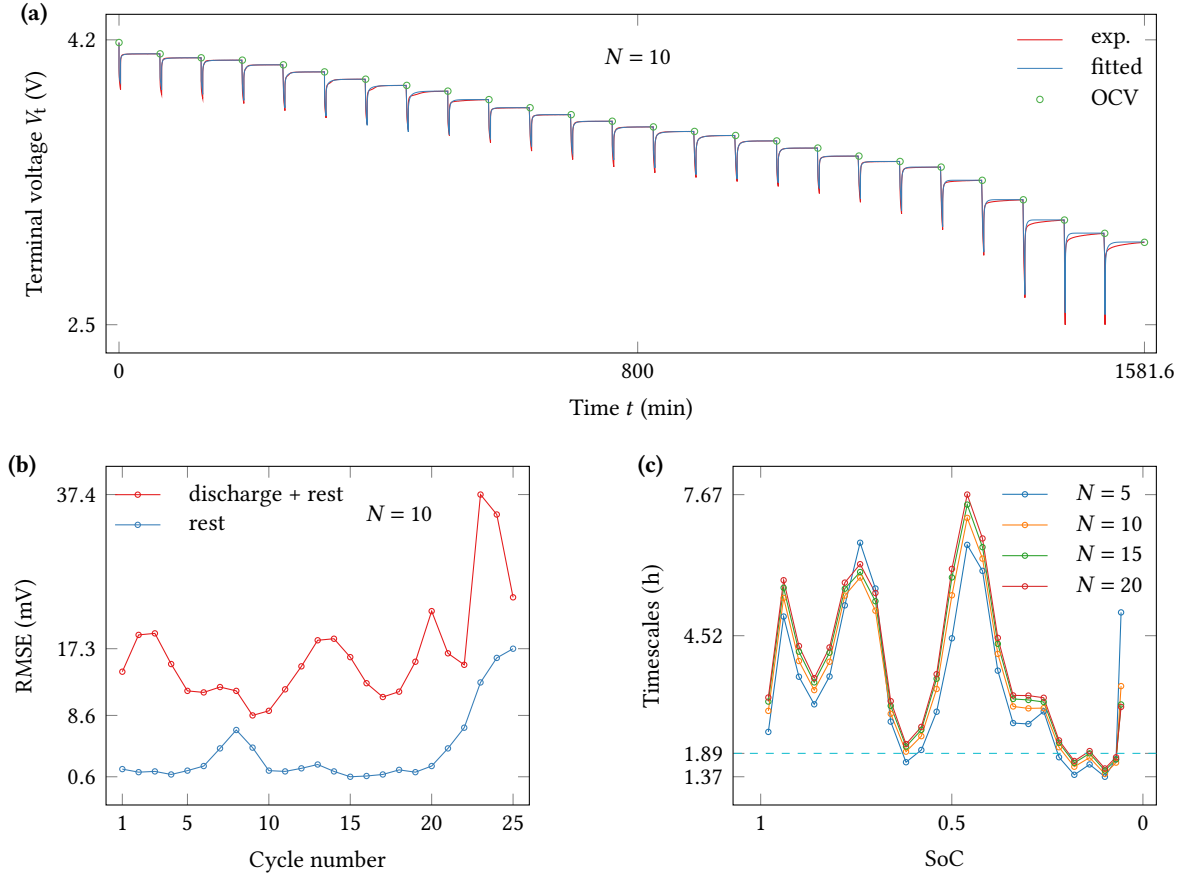


Fig. 8. (a) Best-fitting curve against measured data with calculated R_0 and fitted $R_{d,1}$. (b) Root mean square errors of the best-fitting curve for each discharge-rest segment. (c) Diffusion timescales in Eq. (31) derived from the fitted diffusion resistances. For the timescale estimation, we explored the effect of layer number; otherwise, 10 layers are used elsewhere.

that the difference caused by number of layers is negligible, confirming that the layer number does not change the physics but affects the solution accuracy.

Fig. 9a shows the evolution of the SoC of each layer as well as the cell average SoC at the fitted diffusion resistance. The average SoC decreases during the discharge pulse and then remains unchanged during the rest period; this pattern is repeated from segment to segment. A typical segment (the fifth) is then demonstrated in Fig. 9b. The outermost layer (10th) is characterized by the fastest decrease of SoC in the beginning of the discharge pulse, while the innermost layer does not lose any lithium, forming a concentration gradient inside the particle. After the current is turned off, the concentration in the outermost layer immediately starts to increase while lithium keeps flowing from the inner layers to the outer layers towards an equilibrium. The derivative of the concentration with respect to time is proportional to the current flowing out from each layer in Fig. 9c. The current I_{10} flowing out the 10th layer contributes most to the discharge pulse, followed by the 9th layer. The sudden drop of I_{10} at 256 min from a positive (discharge) value to a negative (charge) one explains the sharp reversing of SoC_{10} in Fig. 9b. The difference between SoC_{10} and the average SoC is responsible for the diffusion overpotential, because that SoC_{10} is close to the surface SoC.

4.2. Prediction

In this section, we use the calibrated two parameters (R_0 and $R_{d,1}$) to predict the cell performance in constant-current discharge tests and compare with the experimental data. The two datasets in Fig. 7b and c, expressing the dependency of $R_{d,1}$ and R_0 on the cell SoC, are fitted by quadratic functions using the least-squares method. The quadratic fitting in Fig. 7b smoothes out the diffusion “spikes” (also reported in Fig. 6 of [20]) in order to match with the smooth voltage curves in Fig. 10a. The two best fits (green solid lines) are then used in the shell ECM. Since these parameters are obtained from GITT data at a 1 C discharge rate, we pick two other rates, 0.4 C and 2 C, for the constant-current discharges.

The model prediction are presented in Fig. 10a, in comparison with the experimental measurements. The estimation error $V_{\text{pre}} - V_{\text{exp}}$, the difference between the predicted terminal voltage and measured voltage, is found to be restricted to the interval ± 0.1 V, as shown in Fig. 10b. The prediction captures the trend of the terminal voltage variation at a low and a high current rate, suggesting that the two overpotentials caused by ohmic resistance and diffusion are the major contributions to the terminal voltage variation. The predicted voltage curves are not as smooth as the experimentally measured curves at the two discharge rates; this is however expected and does not affect the results and interpretation. The voltage curves are based on the dashed OCV curve in Fig. 10a, which is linearly interpolated from the 25 discrete OCV data

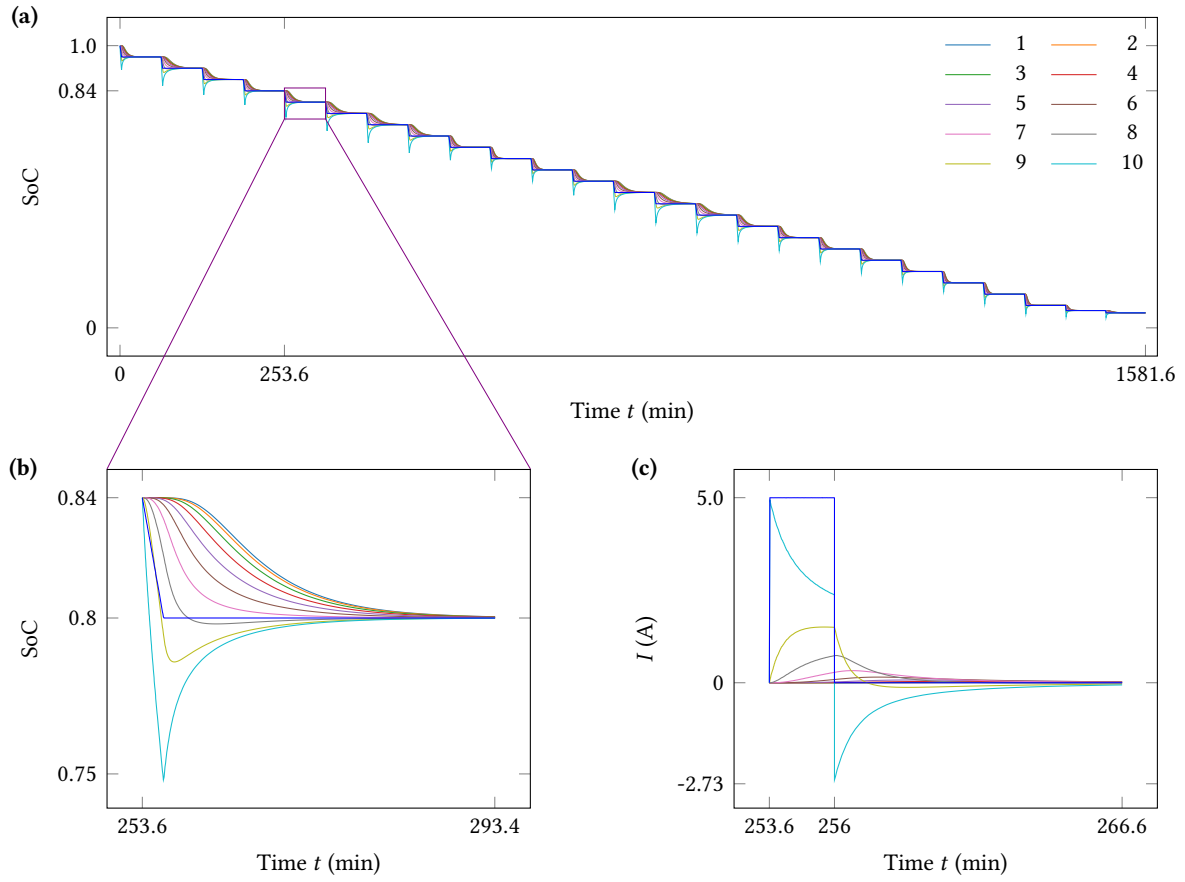


Fig. 9. Evolution of the SoC of each layer and the average SoC (a), and the fifth discharge-rest segment is magnified in (b) for clarity. The corresponding current outflow from each layer is plotted in (c), where the sign of current is opposite to that in Fig. 2. Note that the diffusion-aware voltage source, as well as the associated particle, represents the collective effects of both electrodes.

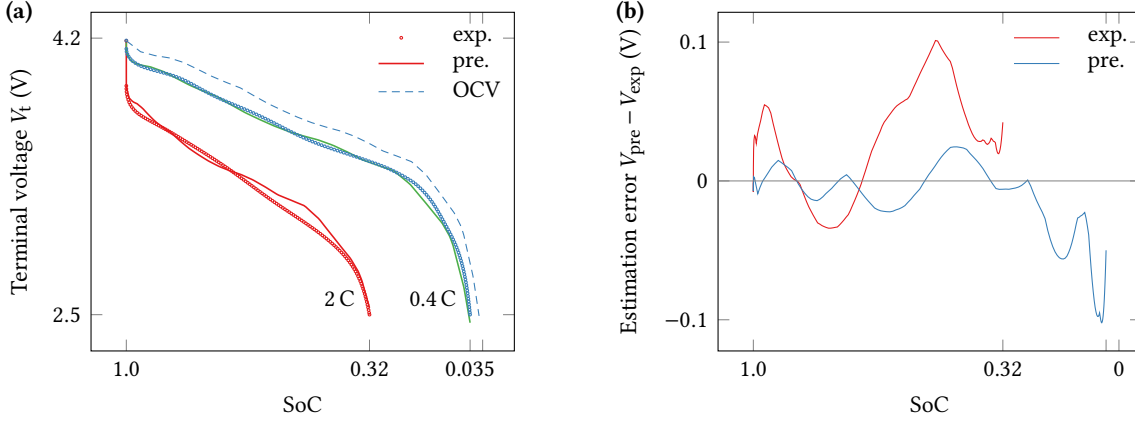


Fig. 10. Comparison between the shell ECM prediction and experimental data.

points in the GITT data in Fig. 8a. Further smoothing of these OCV data points would lead to a smoother OCV curve and smoother voltage curves. Finally, we remark that the rest time (one hour) between two consecutive discharge pulses is relatively short and thus the obtained OCV points especially in the low SoC region may not correspond to the cell equilibrium states, lowering the prediction accuracy.

5. Implementation into battery management systems

In this section, we implement the shell ECM into a battery management system (BMS) and evaluate its performance in comparison with a traditional ECM. Specifically, the implementation is achieved within the closed-loop state estimation BMS of WAE Technologies (WAE). Traditional ECMs are implemented in present-day onboard battery management algorithms to maintain low computational cost, and they have been proven to work well for model-based power limits estimation [23]. To evaluate the viability of the shell ECM for practical onboard usage, we test the shell ECM within the WAE power limits algorithm in a model-in-the-loop testing environment and compare the computational time incurred by the shell ECM with that by the traditional ECM.

The shell ECM and traditional ECM we implemented are sketched in Fig. 11. The shell ECM here differs from the SPM-equivalent one (Fig. 3b) in that it uses an RC pair (charge transfer resistor R_{ct} and double layer capacitor C_{dl}) to account for the fast dynamics and an ohmic resistor R_0 for the overpotential contributed by electronic current flow in the solid and ionic current flow in the electrolyte. The diffusion-aware voltage source for each electrode has 5 layers and thus 5 internal states of concentration to track. For a fair comparison, the traditional ECM also has a symmetrical structure for the two electrodes [24]. Since the traditional voltage source cannot resolve concentration gradient, the diffusion overpotential is

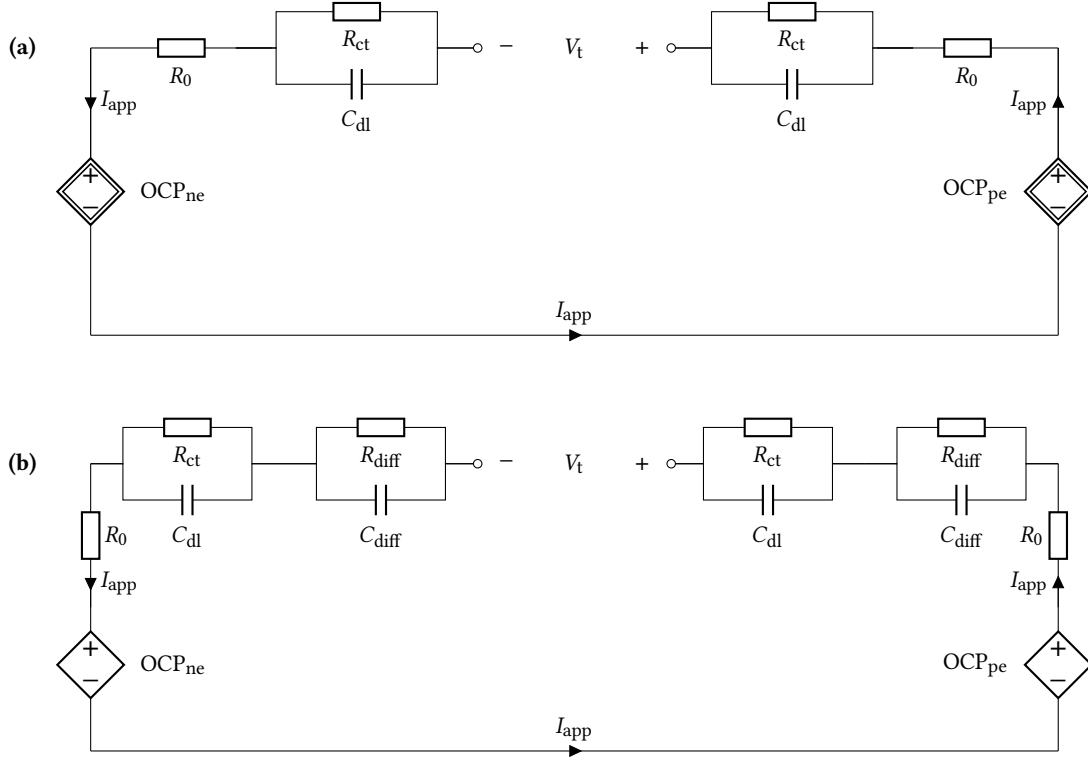


Fig. 11. Configuration of (a) the shell ECM and (b) traditional ECM implemented into WAE Technologies battery management systems.

considered by an additional RC pair (R_{diff} and C_{diff}). The rest is the same as the shell ECM—an RC pair for fast dynamics and an ohmic resistor for instantaneous voltage change.

The two models are parameterized against half-cell pulse data collected from WAE’s physics-based model of the LGM50 cell. The procedures and data for parameterization are the same for both the shell and traditional ECMs. The parameterized shell ECM and traditional ECM are then evaluated in an industrial drive-cycle test. The drive-cycle test data are also generated from WAE’s physics-based model, featuring discharge and regeneration (charge) events (Fig. 13a). In the following, we compare the shell ECM with the traditional ECM in terms of the computational cost and prediction accuracy.

With reference to Fig. 11b, the traditional ECM totalled 10 parameters: 8 for the 4 RC pairs and 2 for the 2 ohmic resistors. It has 5 states to compute: one state for each RC pair and an extra state for the SoC. According to Fig. 11a, the shell model totalled 8 parameters—each diffusion-aware voltage source has one independent diffusion resistance. However, it has 12 states for computation: 2 states for 2 RC pairs, and 10 states for the concentrations in the 10 particle layers (5 for each electrode). Here the SOC of each electrode is calculated based on the volume average of the concentrations in the total 5 layers; unlike the traditional ECM, no state is needed for the average SoC.

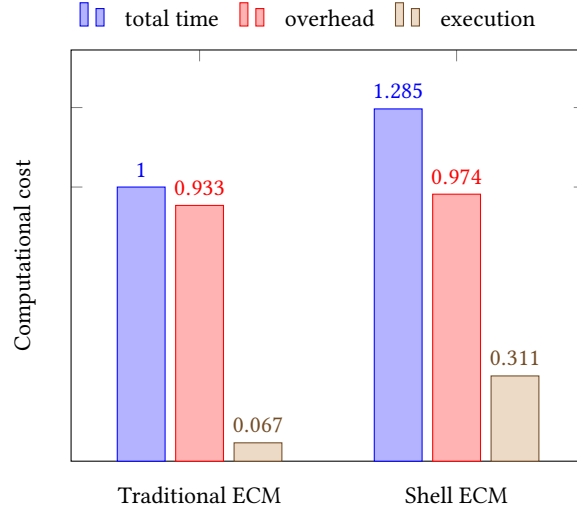


Fig. 12. Computational cost decomposition and comparison between the shell ECM and the traditional ECM. The total computational time is the sum of the model execution time and the overheads by parameter look-up. All the costs are normalized by the total computational time of the traditional ECM.

Fig. 12 shows the computational cost of the two models by profiling analysis. All the computational costs are normalized by the total computational time of the traditional ECM. For both models, the total computational cost is decomposed into the model execution time and parameter lookup overheads. The model execution time of the shell ECM is 4.6 times longer than that of the traditional ECM (0.311 vs 0.067). This is well expected as the shell ECM is equivalent to the discretized diffusion equation and has 12 states to compute. However, in both cases the model execution time is relatively insignificant compared to the overheads by parameter lookup: the execution time is 6.7% and 24.2% of the total computational time for the traditional ECM and shell ECM, respectively. In total, the cost of the shell ECM is 1.3 times the cost of the traditional ECM, when both implemented within a well-developed and computationally efficient BMS. This small increase of overall computational cost is insignificant, in the context of a BMS's total computational overheads. Moreover, the cost of the shell ECM can be further reduced after numerical techniques and layer number are optimized.

The shell ECM shows advantages in terms of prediction accuracy. Fig. 13 shows an overall higher prediction accuracy of the shell ECM compared to the traditional ECM in predicting the terminal voltage of a drive-cycle test. Subplot (a) shows the current evolution, subplot (b) shows the predicted terminal voltages by the two models in comparison with the generated data (cited as target data hereafter) by WAE's physics-based model, and subplot (c) shows the difference between the prediction and target data. It can be seen that large errors of the traditional ECM tend to occur following high current pulses. To confirm this, we further investigate the two models subjected to a charge pulse at a high current rate (2 C) followed by a

rest.

Fig. 14b shows that the shell ECM well captures the terminal voltage during relaxation, while a noticeable discrepancy is observed between the traditional ECM prediction and the target response. The traditional ECM lacks physics; in practice, its parameters are often set to be dependent on the terminal current to maintain a desired level of accuracy when the electrode particle is highly polarized. The current dependency however leads to significant inaccuracy especially during cell relaxation following a charge or discharge: as the current drops close to zero, the model parameters take the values for low current rates, while the large concentration gradient persists. Although numerous attempts have been made to improve the traditional ECM, the above-mentioned issue remains. The shell ECM avoids this issue because it models and tracks the internal concentration states as shown in Fig. 14a, with robustness to dynamic current profiles. Moreover, the parameter of the shell ECM—diffusion resistance—has physical meaning and reduced dependency on external current.

By modeling internal states, the shell ECM enables the application of advanced power limit strategies [6] to improve cell performance and mitigate cell degradation. For example, the surface concentration and diffusion resistance can be used to control power limits based on the anode potential and visibility of internal concentration gradients, as opposed to the cell voltage alone, thus managing lithium plating risk and enabling faster charging [25].

6. Conclusion

We proposed a circuit network (Fig. 2) to describe the lithium diffusion in an active particle, and the proposed circuit network is theoretically and numerically proven equivalent to the discretized diffusion equation based on finite volume method. We define the whole circuit network as a new high-level circuit element, called diffusion-aware voltage source and symbolized by a double-wall diamond (Fig. 3). The diffusion-aware voltage source gives the electrode potential as a function of particle surface concentration, acting as an alternative to the combination of a traditional voltage source and RC pairs in standard ECMs.

Inside the proposed circuit network, the linear dependence of the voltage of each layer on the local concentration/SoC ensures that the concentration gradient is the driving force. The real OCP relation depending on the surface concentration is used as the output of the diffusion-aware voltage source. The diffusion-aware voltage source has been verified by comparison against SPM simulations within PyBaMM, and the simplest shell ECM has been validated by comparison against experimental data.

The value of the work lies in the circuit analogy to the spatially discretized diffusion equation and boundary conditions. This analogy transforms the continuous description of physics-based models into well-

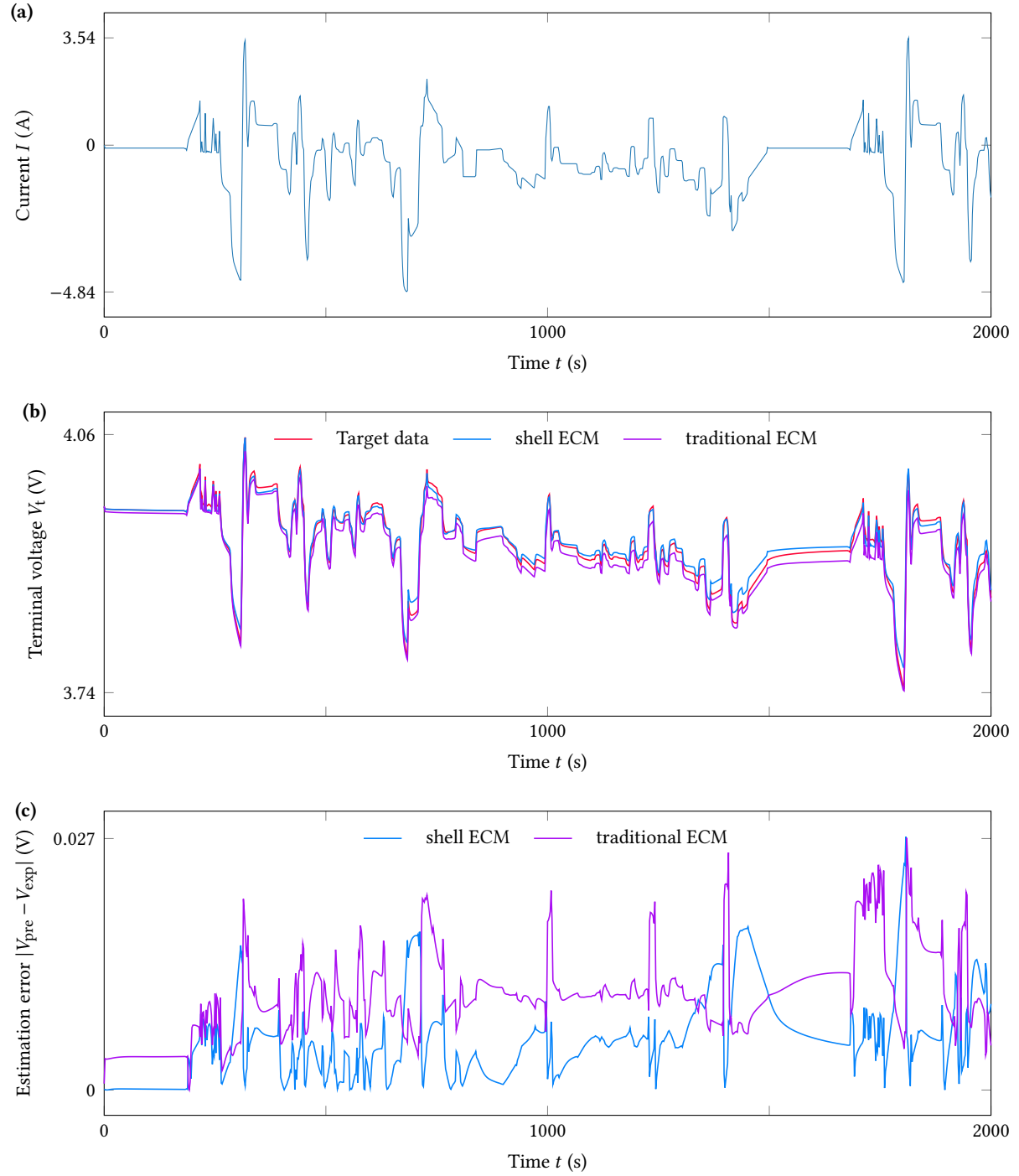


Fig. 13. Comparison of the shell ECM with the traditional ECM in prediction of the terminal voltage (b) of a drive-cycle test with the current profile in subplot (a). The estimation error in subplot (c) is demonstrated as the absolute value of the difference between the prediction and target data, which is generated by WAE's physics-based model.

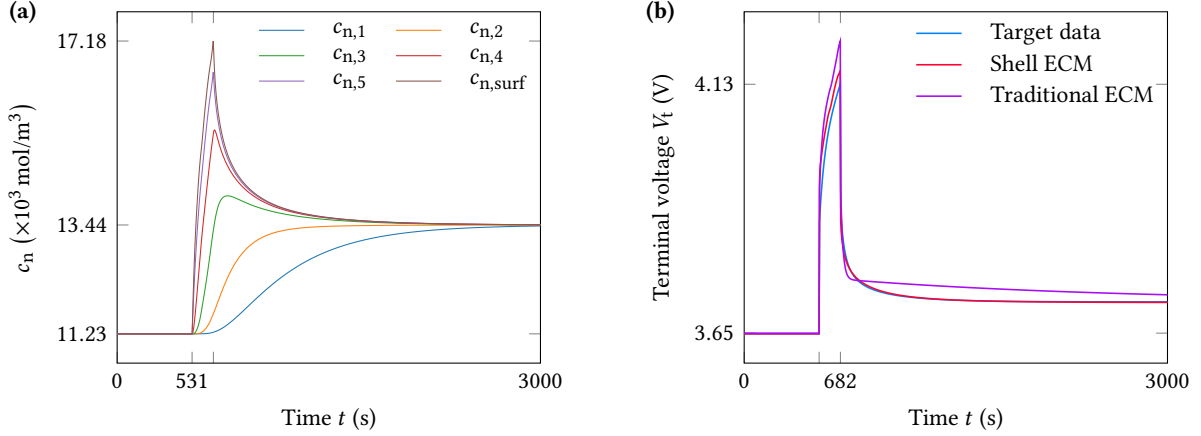


Fig. 14. A test case of 2C charge pulse followed by a rest: (a) the lithium concentration c_n evolution in the 5 layers of negative electrode particle recorded by WAE's battery management system and (b) comparison between the two models in predicting the terminal voltage.

established knowledge/behavior of circuit elements, thereby reducing the implementation complexity for practical on-board usage. Compared to traditional ECMs, the shell ECM containing diffusion-aware voltage sources demands a comparable computational cost, but demonstrates superiority in terms of prediction accuracy and robustness to dynamic current profiles, when both models are tested in a battery management system. By tracking the internal concentration states with a high fidelity, the shell ECM shows great promise in the application of advanced power limit strategies to mitigate cell degradation and enable fast charge.

Acknowledgements

The research leading to these results has received funding from the Innovate UK through the WIZer Batteries project (grant number 104427) and EPSRC Faraday Institution Multi-Scale Modelling project (EP/S003053/1, grant number FIRG025).

Data availability

All relevant data leading to the findings of this study, including parameter values and source codes for model implementation, are openly available in the GitHub repository at <https://github.com/mzzhuo/DAYS>.

Appendix A. Numerical method

This appendix provides numerical procedures to solve the diffusion-aware voltage source as shown in Fig. 2. The diffusion-aware voltage source serves as spatial discretization of the diffusion equation and

converts a partial differential equation into a system of ordinary differential equations. Numerical solutions to ordinary differential equations have been well addressed in textbooks, and open-source solvers are readily available. Depending on desired accuracy and implementation complexity, different methods can be used to solve the system of internal state evolution equations (13).

Here we present the time stepping schemes of the forward and backward Euler methods. The temporal discretization of Eq. (13) for layer n using the forward and backward schemes can be expressed, respectively, as

$$\frac{c_n^{i+1} - c_n^i}{\Delta t} = \frac{1}{F\Omega_n} I_n^i, \quad (\text{A.1})$$

$$\frac{c_n^{i+1} - c_n^i}{\Delta t} = \frac{1}{F\Omega_n} I_n^{i+1}, \quad (\text{A.2})$$

where i denotes the current i -th time step. The forward Euler method (A.1) is an explicit scheme and thus very easy to implement, but it suffers from numerical instability. The stability condition of the forward scheme for states of the diffusion-aware voltage source reads

$$\Delta t \leq \frac{1}{2} \frac{b^2}{D_s}, \quad (\text{A.3})$$

where Δt is the time-step length, b is the thickness of each layer, and D_s is the diffusivity. The backward Euler method (A.2) is more difficult to implement but is free from stability issues. In our case, the diffusivity D_s is constant and thus Eq. (A.2) is a linear system of equations, requiring comparable computational cost compared to the explicit scheme. Both the forward and backward Euler methods are of first-order accuracy; for higher-order accuracy, we can resort to improved Euler method or Runge-Kutta methods.

Appendix B. Experimental method

This appendix details the experimental setup for the measured data presented in Section 4. Experiments were performed on LG M50 (LG GBM50T2170) cylindrical lithium-ion battery cells. All electrochemical data was recorded by a Biologic BCS-815 battery cycler with the accompanying BT-Lab software. The temperature of the cell was recorded using K-type thermocouples adhered to the cell surface using Kapton tape, approximately halfway along the axial direction. These thermocouples were connected to the built-in thermocouple readers of the BCS-815 battery cycler, with temperature data recorded alongside the electrochemical data.

Experiments at the low discharge rate (0.4C) were performed with the cell housed inside a binder thermal

chamber (KB 23 cooling incubator), set to maintain a stable air temperature of 25 °C. The fan speed of the thermal chamber was set to 100%, and the cell was placed in a regime cooled by forced air convection. Electrical connections to the cell were made via a spring-loaded cell holder, which provided a 4-point connection via banana plugs. Connection resistances were not compensated in subsequent tests.

Experiments at higher discharge rates (1C and 2C) were performed with the cell in a conductive cooling regime in order to limit the temperature rise. The cell was in direct thermal contact with aluminium blocks, which had been machined to fit around the cylindrical surface of the cell. Thermal interface material was used to improve heat transfer between the cell and the blocks. The aluminium blocks were held at a constant temperature of 25°C using a bespoke temperature controller. The temperature controller used Peltier elements to heat/cool the blocks based on a PID control, with K-type thermocouples providing feedback. The design of these controllers is described in more details in our previous work [26]. Electrical connections to the cell were made via spot-welded nickel strips which were clamped between brass blocks, and the brass blocks were connected to the battery cycler through banana plugs.

Appendix C. Diffusion timescale estimation

This appendix introduces the derivation of Eq. (31): how to estimate the diffusion timescale (including diffusivity) from the fitted diffusion resistance? In Section 4.1, the parameter $R_{d,1}$ of the diffusion-aware voltage source (Fig. 3c) is fitted against experimental GITT data (Fig. 7). Note that the single diffusion-aware voltage source represents the collective diffusion effect of both electrodes, and at this stage we have information of neither electrode in terms of the size and number of active particles. We thus take the local SoC z_n as the internal state for layer n that is calculated as

$$\frac{dz_n}{dt} = \frac{I_n}{Q_n}, \quad (\text{C.1})$$

where Q_n is the volume-weighted fraction of the cell nominal capacity Q . We re-define the controlled voltage as

$$V_n = kz_n, \quad (\text{C.2})$$

and substitute it into Eq. (10), leading to

$$I_n = \frac{z_{n+1} - z_n}{R_{d,n}/k} - \frac{z_n - c_{z-1}}{R_{d,n-1}/k}. \quad (\text{C.3})$$

Eqs. (C.1) to (C.3) are complete to fit the diffusion resistance $R_{d,1}$ with a given applied current I_{app} as the input.

To estimate the diffusion timescale, we need to relate the fitted diffusion resistance in Eq. (C.3) to the diffusivity in the discretized diffusion equation (7). The cell nominal capacity is assumed to be equal to the capacity of either electrode and estimated as

$$Q = Fc_{s,max}\Omega N_a, \quad (C.4)$$

where Ω is the active particle volume. This relation holds for either of the two electrodes. Accordingly, the nominal capacity for layer n is $Q_n = Fc_{s,max}\Omega_n N_a$, and Eq. (C.1) can thus be reformulated as

$$I_n = Fc_{s,max}N_a \frac{dz_n}{dt} \Omega_n. \quad (C.5)$$

Dividing both sides of Eq. (7) by $c_{s,max}$ and assuming $c_n/c_{s,max}$ is equivalent to the local SoC z_n in Eq. (C.1), we obtain

$$\frac{dz_n}{dt} \Omega_n = \frac{z_{n+1} - z_n}{b/(S_n D_s)} - \frac{z_n - z_{n-1}}{b/(S_{n-1} D_s)}. \quad (C.6)$$

Substituting Eq. (C.6) into Eq. (C.5) and then comparing with Eq. (C.3), we relate the fitted diffusion resistance to the diffusivity:

$$R_{d,n} = \frac{kb}{Fc_{s,max}N_a S_n D_s}. \quad (C.7)$$

Following the same procedures as in Eqs. (14), (19) and (20) leads to Eq. (31) and the expression of diffusivity in terms of the fitted resistance:

$$D_s = \frac{kN}{4\pi Fc_{s,max}N_a a R_{d,1}}. \quad (C.8)$$

References

- [1] G. L. Plett, Battery Management Systems, Volume I: Battery Modeling, Artech House Publishers, 2015.
- [2] M. Weiss, R. Ruess, J. Kasnatscheew, Y. Levartovsky, N. R. Levy, P. Minnmann, L. Stolz, T. Waldmann, M. Wohlfahrt-Mehrens, D. Aurbach, M. Winter, Y. Ein-Eli, J. Janek, Fast charging of lithium-ion

- batteries: A review of materials aspects, *Advanced Energy Materials* 11 (33) (2021) 2101126. doi:[10.1002/aenm.202101126](https://doi.org/10.1002/aenm.202101126).
- [3] M. Doyle, T. F. Fuller, J. Newman, Modeling of galvanostatic charge and discharge of the lithium/polymer/insertion cell, *Journal of The Electrochemical Society* 140 (6) (1993) 1526. doi:[10.1149/1.2221597](https://doi.org/10.1149/1.2221597).
- [4] Y. Yin, Y. Hu, S.-Y. Choe, H. Cho, W. T. Joe, New fast charging method of lithium-ion batteries based on a reduced order electrochemical model considering side reaction, *Journal of Power Sources* 423 (2019) 367–379. doi:[10.1016/j.jpowsour.2019.03.007](https://doi.org/10.1016/j.jpowsour.2019.03.007).
- [5] N. A. Chaturvedi, R. Klein, J. Christensen, J. Ahmed, A. Kojic, Algorithms for advanced battery-management systems, *IEEE Control Systems Magazine* 30 (3) (2010) 49–68. doi:[10.1109/mcs.2010.936293](https://doi.org/10.1109/mcs.2010.936293).
- [6] L. Zheng, J. Zhu, G. Wang, D. D.-C. Lu, T. He, Lithium-ion battery instantaneous available power prediction using surface lithium concentration of solid particles in a simplified electrochemical model, *IEEE Transactions on Power Electronics* 33 (11) (2018) 9551–9560. doi:[10.1109/tpe.2018.2791965](https://doi.org/10.1109/tpe.2018.2791965).
- [7] S. Raël, M. Hinaje, Using electrical analogy to describe mass and charge transport in lithium-ion batteries, *Journal of Power Sources* 222 (2013) 112–122. doi:[10.1016/j.jpowsour.2012.08.071](https://doi.org/10.1016/j.jpowsour.2012.08.071).
- [8] R. Scipioni, P. S. Jørgensen, C. Graves, J. Hjelm, S. H. Jensen, A physically-based equivalent circuit model for the impedance of a LiFePO_4 /graphite 26650 cylindrical cell, *Journal of The Electrochemical Society* 164 (9) (2017) A2017–A2030. doi:[10.1149/2.1071709jes](https://doi.org/10.1149/2.1071709jes).
- [9] M.-T. von Srbik, M. Marinescu, R. F. Martinez-Botas, G. J. Offer, A physically meaningful equivalent circuit network model of a lithium-ion battery accounting for local electrochemical and thermal behaviour, variable double layer capacitance and degradation, *Journal of Power Sources* 325 (2016) 171–184. doi:[10.1016/j.jpowsour.2016.05.051](https://doi.org/10.1016/j.jpowsour.2016.05.051).
- [10] Y. Merla, B. Wu, V. Yufit, R. F. Martinez-Botas, G. J. Offer, An easy-to-parameterise physics-informed battery model and its application towards lithium-ion battery cell design, diagnosis, and degradation, *Journal of Power Sources* 384 (2018) 66–79. doi:[10.1016/j.jpowsour.2018.02.065](https://doi.org/10.1016/j.jpowsour.2018.02.065).
- [11] K. Sato, A. Kono, H. Urushibata, Y. Fujita, M. Koyama, Physics-based model of lithium-ion batteries running on a circuit simulator, *IEEJ Transactions on Industry Applications* 139 (5) (2019) 523–534. doi:[10.1541/ieejias.139.523](https://doi.org/10.1541/ieejias.139.523).

- [12] Y. Li, M. Vilathgamuwa, T. Farrell, S. S. Choi, N. T. Tran, J. Teague, A physics-based distributed-parameter equivalent circuit model for lithium-ion batteries, *Electrochimica Acta* 299 (2019) 451–469. doi:[10.1016/j.electacta.2018.12.167](https://doi.org/10.1016/j.electacta.2018.12.167).
- [13] Z. Geng, S. Wang, M. J. Lacey, D. Brandell, T. Thiringer, Bridging physics-based and equivalent circuit models for lithium-ion batteries, *Electrochimica Acta* 372 (2021) 137829. doi:[10.1016/j.electacta.2021.137829](https://doi.org/10.1016/j.electacta.2021.137829).
- [14] V. R. Subramanian, V. D. Diwakar, D. Tapriyal, Efficient macro-micro scale coupled modeling of batteries, *Journal of The Electrochemical Society* 152 (10) (2005) A2002. doi:[10.1149/1.2032427](https://doi.org/10.1149/1.2032427).
- [15] M. Ouyang, G. Liu, L. Lu, J. Li, X. Han, Enhancing the estimation accuracy in low state-of-charge area: A novel onboard battery model through surface state of charge determination, *Journal of Power Sources* 270 (2014) 221–237. doi:[10.1016/j.jpowsour.2014.07.090](https://doi.org/10.1016/j.jpowsour.2014.07.090).
- [16] Y. Zheng, W. Gao, X. Han, M. Ouyang, L. Lu, D. Guo, An accurate parameters extraction method for a novel on-board battery model considering electrochemical properties, *Journal of Energy Storage* 24 (2019) 100745. doi:[10.1016/j.est.2019.04.019](https://doi.org/10.1016/j.est.2019.04.019).
- [17] V. Sulzer, S. G. Marquis, R. Timms, M. Robinson, S. J. Chapman, Python battery mathematical modelling (PyBaMM), *Journal of Open Research Software* 9 (2021). doi:[10.5334/jors.309](https://doi.org/10.5334/jors.309).
- [18] F. B. Planella, W. Ai, A. M. Boyce, A. Ghosh, I. Korotkin, S. Sahu, V. Sulzer, R. Timms, T. G. Tranter, M. Zyskin, S. J. Cooper, J. S. Edge, J. M. Foster, M. Marinescu, B. Wu, G. Richardson, A continuum of physics-based lithium-ion battery models reviewed, *Progress in Energy* 4 (4) (2022) 042003. doi:[10.1088/2516-1083/ac7d31](https://doi.org/10.1088/2516-1083/ac7d31).
- [19] C. H. Chen, F. B. Planella, K. O'Regan, D. Gastol, W. D. Widanage, E. Kendrick, Development of experimental techniques for parameterization of multi-scale lithium-ion battery models, *Journal of The Electrochemical Society* 167 (8) (2020) 080534. doi:[10.1149/1945-7111/ab9050](https://doi.org/10.1149/1945-7111/ab9050).
- [20] K. O'Regan, F. B. Planella, W. D. Widanage, E. Kendrick, Thermal-electrochemical parameters of a high energy lithium-ion cylindrical battery, *Electrochimica Acta* 425 (2022) 140700. doi:[10.1016/j.electacta.2022.140700](https://doi.org/10.1016/j.electacta.2022.140700).
- [21] S. G. Marquis, V. Sulzer, R. Timms, C. P. Please, S. J. Chapman, An asymptotic derivation of a single particle model with electrolyte, *Journal of The Electrochemical Society* 166 (15) (2019) A3693–A3706. doi:[10.1149/2.0341915jes](https://doi.org/10.1149/2.0341915jes).

- [22] M. Doyle, J. Newman, A. S. Gozdz, C. N. Schmutz, J.-M. Tarascon, Comparison of modeling predictions with experimental data from plastic lithium ion cells, *Journal of The Electrochemical Society* 143 (6) (1996) 1890–1903. [doi:10.1149/1.1836921](https://doi.org/10.1149/1.1836921).
- [23] G. L. Plett, High-performance battery-pack power estimation using a dynamic cell model, *IEEE Transactions on Vehicular Technology* 53 (5) (2004) 1586–1593. [doi:10.1109/tvt.2004.832408](https://doi.org/10.1109/tvt.2004.832408).
- [24] C. Zhang, T. Amietszajew, S. Li, M. Marinescu, G. Offer, C. Wang, Y. Guo, R. Bhagat, Real-time estimation of negative electrode potential and state of charge of lithium-ion battery based on a half-cell-level equivalent circuit model, *Journal of Energy Storage* 51 (2022) 104362. [doi:10.1016/j.est.2022.104362](https://doi.org/10.1016/j.est.2022.104362).
- [25] M. A. Xavier, A. K. de Souza, K. Karami, G. L. Plett, M. S. Trimboli, A computational framework for lithium ion cell-level model predictive control using a physics-based reduced-order model, *IEEE Control Systems Letters* 5 (4) (2021) 1387–1392. [doi:10.1109/lcsys.2020.3038131](https://doi.org/10.1109/lcsys.2020.3038131).
- [26] N. Kirkaldy, M. A. Samieian, G. J. Offer, M. Marinescu, Y. Patel, Lithium-ion battery degradation: Measuring rapid loss of active silicon in silicon–graphite composite electrodes, *ACS Applied Energy Materials* (2022). [doi:10.1021/acsaem.2c02047](https://doi.org/10.1021/acsaem.2c02047).